Biosensors and Bioelectronics 150 (2020) 111875

Contents lists available at ScienceDirect

Biosensors and Bioelectronics

journal homepage: http://www.elsevier.com/locate/bios

Highly sensitive photoelectrochemical detection of bleomycin based on Au/WS_2 nanorod array as signal matrix and Ag/ZnMOF nanozyme as multifunctional amplifier

Weisu Kong [a], Xiaoxi Guo [a], Man Jing [a], Fengli Qu [a,*], Limin Lu [b,**]

[a] College of Chemistry and Chemical Engineering, Qufu Normal University, Qufu, Shandong, 273165, PR China
[b] Institute of Functional Materials and Agricultural Applied Chemistry, College of Science, Jiangxi Agricultural University, Nanchang, 330045, PR China

ARTICLE INFO

Keywords:
Photoelectrochemical
Bleomycin
WS_2 nanorod array
Ag/ZnMOF nanozyme

ABSTRACT:

An ultrasensitive photoelectrochemical (PEC) biosensor was constructed based on gold nanoparticles (Au NPs)/tungsten sulfide nanorod array (WS_2 NA) photoelectrode as the PEC matrix and silver nanoparticles/flake-like zinc metal-organic framework (Ag/ZnMOF) nanozyme with the peroxidase mimetic enzyme property for sensitive detection of bleomycin (BLM). In particular, Au/WS_2 and Ag/ZnMOF were linked by thiolate DNA_1 and DNA_2 strand, respectively, and the Au/WS_2–Ag/ZnMOF probe was prepared via hybridization reaction between the two DNAs. The introduction of Ag/ZnMOF in the probe offers two functions: i) the steric hindrance effect can effectively impede electron transport and reduce the photocurrent; ii) Ag/ZnMOF nanozyme can also be used as mimic peroxidase to effectively catalyze 3,3-diaminobenzidine (DAB) to produce the relevant precipitation, which will further reduce photocurrent and eliminate false positive signals. When BLM exists, BLM with Fe^{2+} as irreversible cofactor can specifically recognize and cleave of the 5′-GC-3′ active site of DNA_2, resulting in reduced precipitation deposited on the electrode and recovery of PEC signal. The highly sensitive PEC biosensor exhibits a the linear strategy from 0.5 nM to 500 nM with a detection limit down to 0.18 nM. Further, the unique strategy was conducted in biological samples for BLM detection with satisfactory consequence, offering available and efficient pathway for disease diagnosis.

1. Introduction

Bleomycin (BLM), a class of natural glycopeptide derived antibiotics, has been extensively used as an anticancer drug for different kinds of cancers, including squamous cell carcinoma, Hodgkin's disease, and cervical cancer (Claussen et al., 1999; Galm et al., 2005; Bayer et al., 1992). The antitumor activity of BLM generally relies on the dissociation of DNA caused by the binding between BLM and a metal ion (Fe^{2+}) in a low oxidation state (Claussen et al., 1999; Stubbe et al., 1987). Nevertheless, the improper use of BLM in clinical application can cause some serious consequences, such as pulmonary fibrosis, the toxicity of kidney and lung (Sleijfer et al., 2001). So far, a variety of analytical methods have been constructed for BLM detection, including electrochemical, fluorescence and electrogenerated chemiluminescence (Ma et al., 2018; Li et al., 2013; Yin et al., 2010) etc. However, the above methods are generally affected by complicated operations, low sensitivity and high cost. It is urgent to develop a sensitive and efficient method for quantitative determination of BLM in chemotherapeutic drugs and clinical samples.

As a novel analytical method, photoelectrochemical (PEC) sensing has attracted vital attentions for the past few years. It can achieve the absolute separation of the input signal and the output signal, which takes the advantages of low background signal, high detection sensitivity, low-cost determination and fast response (Zhao et al., 2016; Kong et al., 2019). Until now, the PEC bioanalysis has been widely used to detect DNA (Li et al., 2018a; Wang et al., 2018a), proteins (Ma et al., 2015, 2016), enzymatic activity (Zhang et al., 2018), and cancer cells (Liu et al., 2018; Wang et al., 2018b; Wu et al., 2018) etc. Various functional nanomaterials, including metal-based semiconductor nanomaterials (Gill et al., 2008; Li et al., 2016b; Han et al., 2018), carbon nanomaterials (Hu et al., 2013), and some nanocomplexes (Tang et al., 2014; Hao et al., 2017), have been developed for fabricating PEC sensing

* Corresponding author.
** Corresponding author.
E-mail addresses: fengliquhn@hotmail.com (F. Qu), lulimin816@hotmail.com (L. Lu).

https://doi.org/10.1016/j.bios.2019.111875
Received 29 August 2019; Received in revised form 30 October 2019; Accepted 11 November 2019
Available online 13 November 2019
0956-5663/

platforms, which can convert light illumination into an electrical signal. Under the condition of illumination, the electrons transfer from the valence band (VB) to the conduction band (CB), resulting in the separation of photogenerated electrons and holes (Liu et al., 2017). Many three-dimensional (3D) nanomaterials, such as sulfide materials, carbon-based materials and oxide materials, have been synthesized and investigated (Zhu et al., 2019; Chen et al., 2018; You et al., 2018). Due to their high orientation, large specific surface area and uniform interfacial structure, 3D nanoarrays have attracted extensive research interest as PEC matrices. Among the variety of 3D nanoscale sulfide, the tungsten sulfide nanorod array on Ti mesh (WS_2 NA/TM) has the advantages of high active site density, good stability, and good electrolyte diffusion, which is beneficial to generate PEC signals (Zhang et al., 2012). In addition, the synthesis of metal/semiconductor heterostructures can significantly improve visible light absorption (Liu et al., 2011; Seh et al., 2012; Li et al., 2014). Among them, the localized surface plasmon resonance (LSPR) effect of gold nanoparticles (Au NPs) can induce charge-transfer, further improving the electron separation efficiency of PEC nanophase materials (Yan et al., 2016a, 2016b). Therefore, we expect Au NPs to be combined with WS_2 NA to further improve PEC performance.

Natural enzymes can catalyze the production of insoluble precipitation for specific substances to achieve signal amplification. For instance, horseradish peroxidase (HRP) can expedite the oxidation for 3,3-diaminobenzidine (DAB) to produce insoluble precipitates (Cui et al., 2018). Nevertheless, natural enzymes encounter the disadvantages of instability, high production costs and rigorous storage conditions, which limit its wide use (Cui et al., 2011). Some nanomaterials-based enzyme mimetics were developed by controllable synthesis with high catalytic activity and low production costs. Highly reductive silver nanoparticles (Ag NPs) are highly efficient, stable and easily prepared mimetic enzyme. For example, Chang's group reported that Au/Ag composite as the mimic peroxidase can effectively catalyze some reactions (Wang et al., 2012). Metal-organic frameworks (MOFs) are constructed from metal ions and organic ligands via coordination bonds, which have superior catalytic activity owing to the ordered stable porous structure and great surface area. However, the MOFs structure with low density of atoms reduce their active sites and adsorption capacity (Li et al., 2016a; Huang et al., 2017). The highly reductive Ag NPs are uniformly deposited on the surface of MOFs, which not only eliminates the main defects of MOFs, but also avoids agglomeration of Ag NPs, increases active sites, and improves catalytic activity (Bagheri et al., 2018).

Herein, we report a novel, low-cost PEC analysis method for ultrasensitive detection of BLM using a highly active Ag/ZnMOF nanozyme with the peroxide mimetic enzyme property as a signal amplifier and Au/WS_2 photoelectrode as a PEC matrix, respectively. In detail, the WS_2 NA with a narrow direct band gap of 2.0 eV can be excited by visible light to produce high photocurrent (Zhang et al., 2012). The PEC signal and transfer efficiency can be further enhanced by introducing Au NPs on WS_2 NA because of the LSPR (Yan et al., 2016a). Zn-based MOFs were introduced to enhance the nanozyme activity of Ag nanoparticle (Ag/ZnMOF), which can catalyze the reaction of hydrogen peroxide (H_2O_2) and a usual substrate (eg: DAB) to produce the relevant precipitation. This will reduce photocurrent and eliminate false positive signals (Cui et al., 2018; Bagheri et al., 2018). Moreover, the steric hindrance effect of Ag/ZnMOF composite can effectively impede electron transport and further reduce the photocurrent. However, in the presence of BLM, due to the oxidation reaction, the DNA_2 (P2) undergoes the irreversible cleavage with Fe^{2+} as a cofactor, resulting in the decrease of electrode surface precipitation and generation of an enhanced PEC signal. Therefore, Ag/ZnMOF becomes unattached to the electrode surface and the PEC signal is recovered. On the basis of the cooperation of mimicking biocatalytic reaction, the designed PEC biosensing system in this work achieved excellent performance compared to other common PEC sensors.

2. Experimental

2.1. Materials and reagents

Materials and reagents adopted within this research are demonstrated in Supporting Information.

2.2. Apparatus

Apparatus used in this research are provided in Supporting Information.

2.3. Synthesis of materials

Preparation of ZnMOF, Ag@ZnMOF composites, WS_2 NA and DNA_1 (P1)–Au NPs are provided in Supporting Information.

2.4. Fabrication of PEC biosensor

The fixed area of WS_2/TM was 0.5 × 0.5 cm. 10 μL of P1–Au were immobilized on the surface of the WS_2/TM electrode through the Au–S bond and incubated 12 h. After washed with 10 mM Tris-HCl buffer (pH 7.8), the obtained P1–Au/WS_2/TM electrode was passivated with 1 wt% BSA for 30 min. Afterwards, 15 μL of Ag/ZnMOF-P2 were introduced into the sensing platform based on the hybridization reaction of P1 and P2 for 2 h at 37 °C. The obtained electrode (Ag/ZnMOF-P2/BSA/P1–Au/WS_2/TM) was incubated with 1.0 mg mL^{-1} DAB and 10 mM H_2O_2 solution for 5 min to proceed nanozyme-catalyzed precipitation reaction. Then, 10 μL of BLM·Fe^{2+} with different concentrations were added. The PEC performance was tested in 10 mM Tris-HCl buffer (pH 7.8) with switchable light excitation at the applied potential of + 0.3 V (vs Ag/AgCl).

2.5. PEC measurement of BLM activity

The BLM samples were prepared by mixing BLM with Fe^{2+} ions in a molar ratio of 1:1. The reaction solution containing different concentrations of BLM (10 μL) was incubated with a PEC biosensor for 10 min at 37 °C. Then the electrode was washed with 10 mM Tris-HCl buffer (pH 7.8). Subsequently, 5 μL of DAB (1.0 mg mL^{-1}) and 5 μL of H_2O_2 (0.01 M) were dropped on the surface of the electrode for 5 min to allow enzymatic catalytic reaction to take place. After washing with 10 mM Tris-HCl buffer (pH 7.8), the electrode was subjected to PEC measurement.

3. Results and discussion

3.1. Mechanism of electron transfer

The photogenerated electron-hole transfer mechanism of the proposed PEC biosensor is illustrated in Scheme 1B. Under visible light irradiation, WS_2/TM was photoexcited to cause electrons to transition from the VB to the CB, producing electron-hole (e^--h^+) pairs. The LSPR of Au NPs was caused by the collective oscillation of conductive electrons due to the applied electromagnetic field of the incident light (Li et al., 2018b). More importantly, Au NPs have excellent plasma absorption characteristics, strong local electric field and surface visible light-induced charge separation, the photoelectric conversion efficiency is further improved (Kelly et al., 2003). After the Ag/ZnMOF-P2 conjugate was bound to the PEC sensor by the hybridization reaction between P1 and P2, the highly active Ag/ZnMOF nanozyme catalyzes H_2O_2 to oxidize DAB and produces an insulating precipitate on the electrode surface, resulting in blockage of electron transfer.

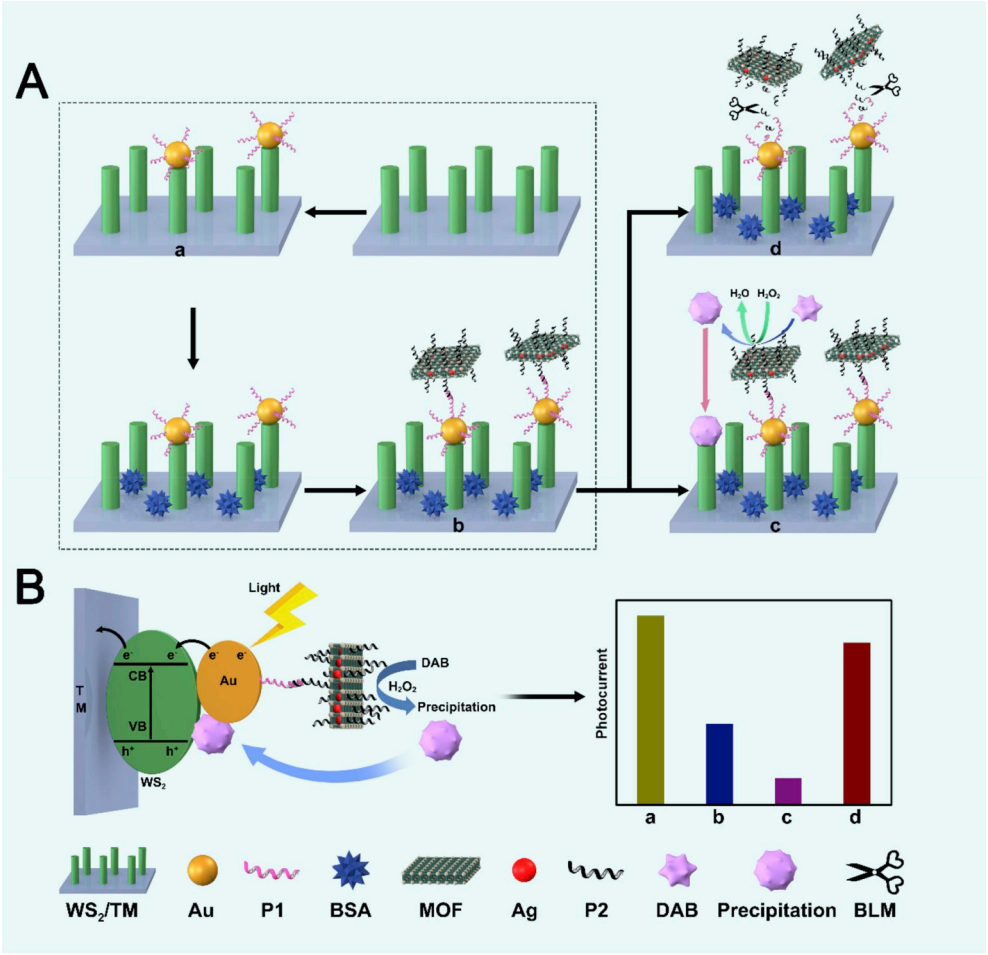

Scheme 1. (A) Schematic illustration of photoelectrochemical biosensor based on Au/WS_2 for BLM detection using a highly active Ag/ZnMOF mimic enzyme as a signal amplifier. (B) Schematic of the charge-carrier transfer process in WS_2 nanorod array and Au nanoparticles. The a, b, c and d in the histogram correspond to Scheme 1A.

3.2. Morphology characterization of WS_2 NA, Au NPs, ZnMOF, and Ag/ZnMOF

The morphology of WS_2 NA, Au NPs, ZnMOF, and Ag/ZnMOF were investigated by SEM and TEM. Fig. 1A shows the SEM image of WS_2 NA, which exhibits a uniform nanorod array state. TEM image of WS_2 NA in Fig. 1B corresponds to Fig. 1A, further revealing the nanorod structure of WS_2. The above characterization demonstrates the successful synthesis of the nanorod arrays. The three-dimensional nanorod array has large surface area, high active site density and good stability, which is beneficial to PEC performance. In addition, the HRTEM image in Fig. 1B inset shows that the interplanar spacing of WS_2 nanorod is 0.618 nm, corresponding to the (002) plane of WS_2. Size and particle distribution of Au NPs were characterized by TEM. As shown in Fig. 1C, the average size of the Au NPs is measured to be about 18 ± 1 nm, which exhibits uniform spherical shape. The uniform distribution of nanoparticles can promote effective photon energy absorption, which is beneficial to LSPR effect. In Fig. 1C inset, the lattice fringe spacing of the Au NPs is estimated to be 0.24 nm, which could be indexed to the Au (111) crystal plane (Wen et al., 2015). The SEM image of ZnMOF is shown in Fig. 1D, suggesting its flake-like structure. The deposition of Ag NPs onto the ZnMOF material is confirmed by the TEM and HRTEM image in Fig. 1E. In Fig. 1E inset, the HRTEM image clearly shows that the Ag NPs (lattice size 0.27 nm) enter the MOF. Furthermore, the energy dispersive X-ray spectrum (EDS) elemental mapping images (Fig. S1) further suggests the uniform distribution of Ag, Zn, C, and O elements in the Ag/ZnMOF. Fig. 1F shows the EDS elemental mapping images of WS_2 NA, which shows the uniform distribution of the W and S elements in the whole nanoarray.

3.3. Compositional and spectroscopic characterization of WS_2/TM, ZnMOF and Ag/ZnMOF

Fig. 2A presents the XRD patterns for WS_2/TM. The diffraction peaks at 14.3°, 33.8°, 39.5°, 49.7°, 55.8°, 58.4°, 60.9° and 61.9° can be indexed to the (002), (101), (103), (105), (106), (008), (112) and (007) planes of WS_2 (JCPDS No. 08-0237), respectively (Wu et al., 2012; Lim et al., 2017). The other peaks correspond to metallic Ti (JCPDS No. 44-1294), these results demonstrate the successful synthesis of the WS_2 NA. (Ren et al., 2017). Elemental composition identification by XPS also further characterizes the composition of different materials. As shown in Fig. S2A, The XPS spectrum of WS_2 NA demonstrates to contain W and S elements. Fig. S2B illustrates the high-resolution XPS spectrum of W 4f, which contains W $4f_{7/2}$ at 32.7 eV and W $4f_{5/2}$ at 34.8 eV, leading to a doublet with an energy gap of approximately 2.2 eV (Pu et al., 2014; Zou et al., 2015). In addition, Fig. S2C presents the S 2p region, the peak at 162.5 eV and 163.5 eV corresponds to S^{2-} state, and the peak at 169.1 eV is assigned to typical W–O–S species caused by surface oxidation in air (Escudero et al., 2016; Du et al., 2018). These results indicate that the formation of WS_2 NA is without any other impurities except for the slight degree of oxidation of WS_2 during the annealing reaction.

FT-IR spectra demonstrate the successful preparation of Ag/ZnMOF. As shown in Fig. 2B, there are characteristic peaks at 1659 and 1570 cm^{-1} of ZnMOF (red line), which is assigned to stretching

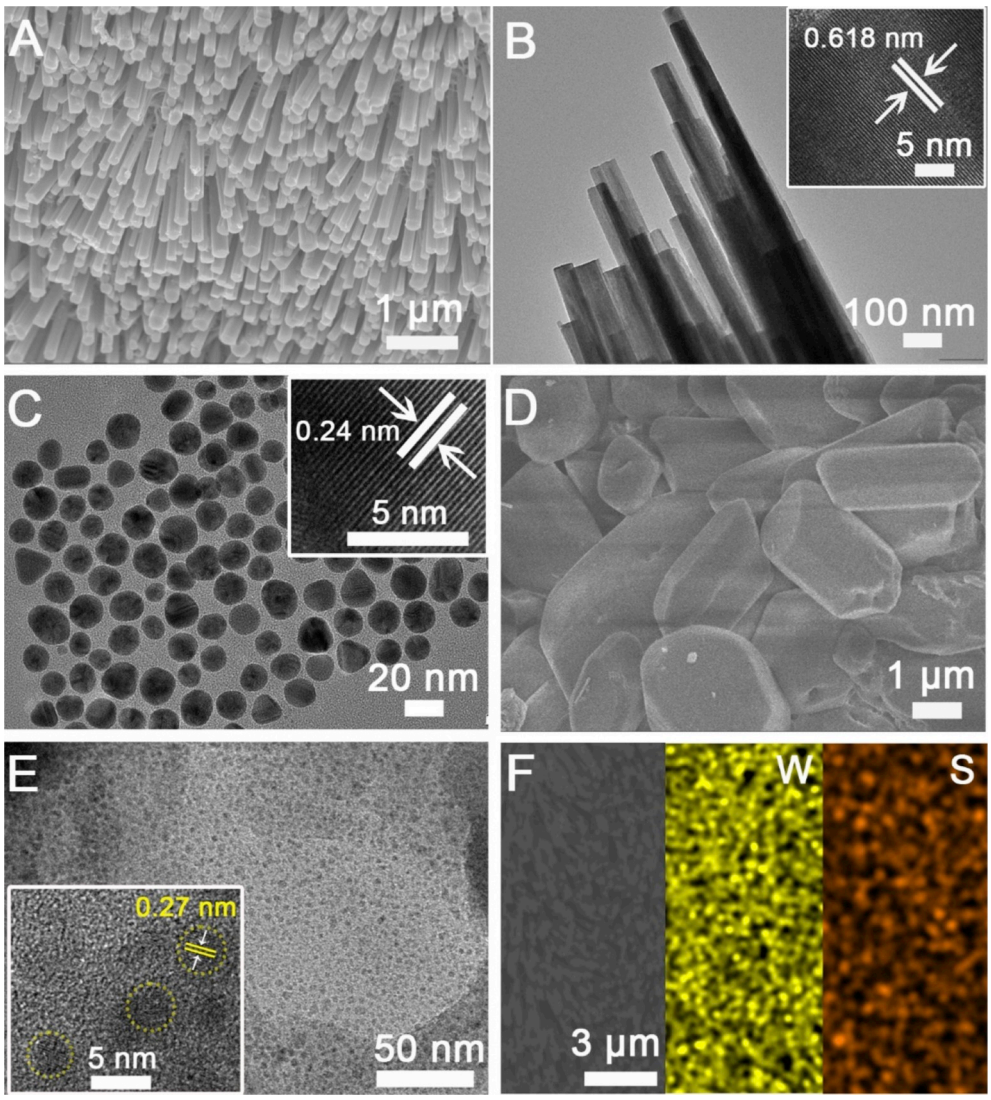

Fig. 1. (A) SEM and (B) TEM image of WS_2 NA, the inset is the HRTEM image of WS_2 NA. (C) TEM image of Au NPs the inset is the HRTEM image of Au NPs. (D) SEM images of ZnMOF. (E) TEM image of Ag/ZnMOF, the inset is the HRTEM image of Ag/ZnMOF and (F) EDS elemental mapping images of WS_2 for W and S elements.

vibration of C═O and C–C bonds of TA linker. In addition, the absorption peaks at about 530 and 1144 cm^{-1} are attributed to Zn–O and C–O bonds in the MOF structure, respectively. The specific peaks at 1048 cm^{-1} and 2969 cm^{-1} are due to C–N and C–H bonds of DMF (chemical structure of prepared MOF). In the FT-IR spectra, some modifications of the Ag/ZnMOF (black line) composite compared to MOF are observed, probably due to the placement of Ag NPs in the MOF pores. The Ag NPs are uniformly deposited in MOFs, which can eliminate the main defects of MOFs and avoid the agglomeration of Ag NPs, increase the active sites and increase the catalytic activity.

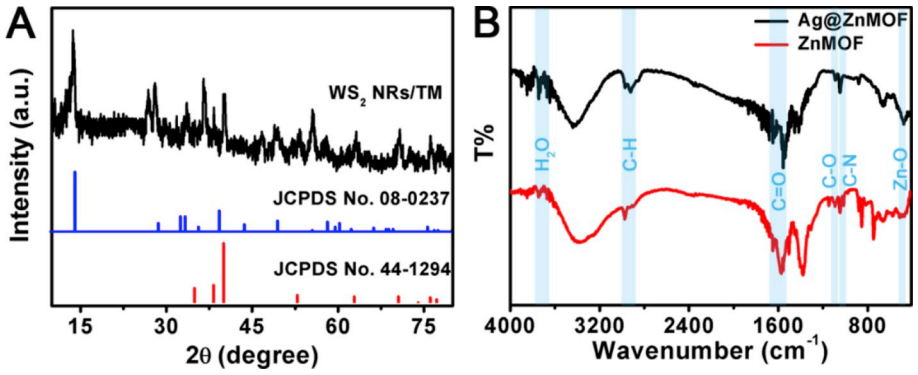

Fig. 2. (A) XRD pattern of pure WS_2 NA. (B) FT-IR spectra of ZnMOF (red) and Ag/ZnMOF (black). (For interpretation of the references to color in this figure legend, the reader is referred to the Web version of this article.)

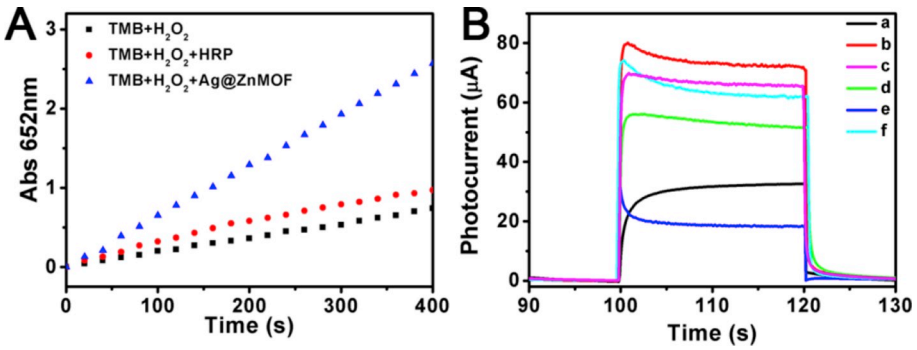

Fig. 3. (A) The time course of UV–vis absorption of the colorimetric reaction of TMB oxidation was monitored at 652 nm with 0.1 mg mL^{-1} Ag@ZnMOF, 0.1 M HRP or blank in 0.1 M HAc-NaAc (pH = 3.5) buffer. The H_2O_2 concentration was 0.1 M. (B) Photocurrent responses in 0.01 M Tris-HCl buffer (pH 7.8), (a) WS_2/TM; (b) P1–Au/WS_2/TM; (c) BSA/P1–Au/WS_2/TM; (d) Ag/ZnMOF-P2/BSA/P1–Au/WS_2/TM; (e) Ag/ZnMOF-P2/BSA/P1–Au/WS_2/TM after incubation with 1.0 mg mL^{-1} DAB and 0.01 M H_2O_2 for 5 min; (f) Ag/ZnMOF-P2/BSA/P1–Au/WS_2/TM after reaction with 1 μM BLM·Fe^{2+} followed by incubation with DAB and H_2O_2.

3.4. Peroxidase mimetic enzyme activity of the Ag@ZnMOF nanozyme

To verify the high activity of the peroxidase mimetic enzyme of Ag@ZnMOF nanozyme, TMB was tested in the catalytic oxidation of peroxidase substrate in the presence of H_2O_2. Fig. 3A shows the time course of the UV–vis absorption curve of the colorimetric reaction. It is apparent that the Ag/ZnMOF nanozyme exhibits a higher reaction rate than HRP and blank. In addition, Ag/ZnMOF can catalyze the oxidation of DAB by H_2O_2 to produce a typical brown solution (Fig. S3c), which is produced by the oxidation product of DAB. Additional control experiments using DAB in the absence of H_2O_2 or Ag/ZnMOF show without color change (Figs. S3a and S3b), indicating that the oxidation reaction required both components to be present. These findings indicate that Ag/ZnMOF has mimic peroxidase catalytic activity.

3.5. PEC and EIS characterization of the constructed PEC biosensors

To illustrate the fabrication of the biosensor, the assembly steps of the sensors were demonstrated by PEC measurements and electrochemical impedance spectroscopy (EIS) under optimal measurement conditions (See the Supporting Information for specific optimization). As shown in Fig. 3B, the WS_2/TM electrode (curve a) exhibits an apparent photocurrent signal (about 31.7 μA), which is shown that WS_2 NA has excellent photoactivity in PEC biosensing applications. After the Au NPs are further modified on the WS_2/TM electrode, the photocurrent is enhanced (curve b, 72.9 μA). Since the LSPR effect of Au NPs promotes the efficiency of electron separation, and plasma energy can be transferred from Au NPs to WS_2 NA (Scheme 1B) to improve PEC performance. Due to the poor steric hindrance charge transfer ability, the photocurrent response is gradually reduced after incubation of BSA and Ag/ZnMOF-P2 on the electrode (curves c and d), which indicates the successful fabrication of immunosensors. In the presence of H_2O_2, the Ag/ZnMOF-P2/BSA/P1–Au/WS_2/TM electrode is incubated with DAB and the PEC signal is significantly reduced to 18.7 μA (curve e) owe to the catalyzed precipitation on the electrode surface. In the presence of BLM with Fe^{2+}, an irreversible scission of P2 is underwent, resulting in the increase of photocurrent to 57.3 μA (curve f). This excellent performance can be attributed to the following reasons: i) In the absence of BLM·Fe^{2+}, Ag/ZnMOF nanozyme with the peroxidase mimetic enzyme property to effectively catalyzes the precipitation of DAB on the sensor surface, which will significantly reduce photocurrent and effectively eliminate false positive signals. ii) In contrast, in the presence of BLM with Fe^{2+}, the BLM·Fe^{2+} complex could selectively cleave the P2 at 5′-GC-3′ scission site, leading to a reduction in catalytic precipitation and generation of a high photocurrent. These results indicate that the PEC biosensor has been successfully constructed according to Scheme 1A and can be used for BLM activity assays.

As shown in Fig. S4, using $[Fe(CN)_6]^{3-/4-}$ as a redox probe to measure EIS. The Nyquist plot at P1–Au/WS_2/TM (curve b) shows a much smaller half-circle diameter than WS_2/TM(curve a), possibly due to the good conductivity of Au NPs improved the electron transfer of $[Fe(CN)_6]^{3-/4-}$ at the electrode surface. After assembling BSA on the P1–Au/WS_2/TM electrode is slight change in the resistance (Ret.) value (curve c). This can be attributed to the insulation effect of proteins hindering the transfer of electrons. In addition, when Ag/ZnMOF-P2 is assembled on the BSA/P1–Au/WS_2/TM electrode, the Ret. increases due to steric hindrance (curve d). After incubation of Ag/ZnMOF-P2/BSA/P1–Au/WS_2/TM with DAB and H_2O_2, Ret. is significantly increased due to the catalytic oxidation of DAB by Ag/ZnMOF of H_2O_2. The transfer of $[Fe(CN)_6]^{3-/4-}$ electrons to the electrode surface (curve e) is hindered by the formation of insoluble insulation. When BLM·Fe^{2+} is added, a significant reduction in Ret. is observed (curve f) owe to BLM·Fe^{2+} specific shearing of P2 to conjugate Ag/ZnMOF-P2 from BSA/P1–Au/WS_2/TM caused by surface dissociation of the electrode. This demonstrates the successful manufacture of PEC biosensors.

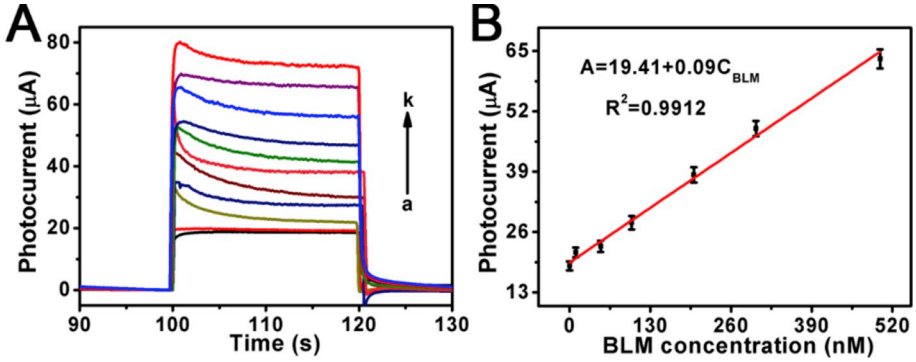

Fig. 4. (A) Photocurrent responses of the different concentration of BLM at + 0.3 V (vs. Ag/AgCl), from a to k: 0, 0.5, 50, 100, 150, 200, 250, 300, 400, 3×10^3 and 1×10^4 nM, respectively. (B) The calibration plot of three replicate determinations at a bias potential of +0.3 V (vs. Ag/AgCl). The error bars were derived from the standard deviation of three measurements. Error bar = SD (n = 3).

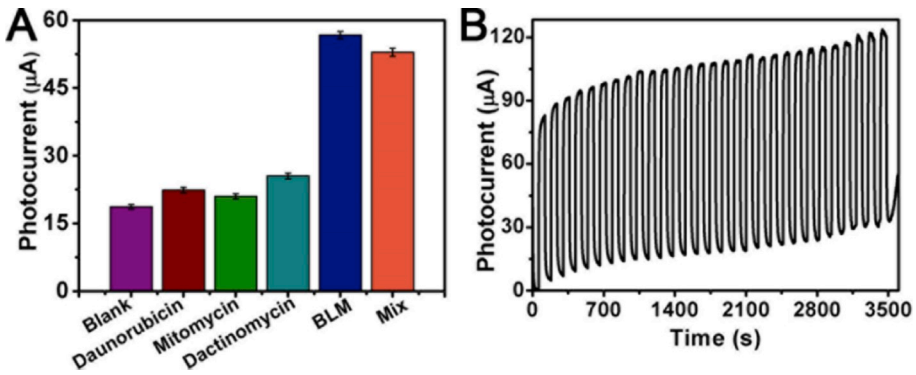

Fig. 5. (A) Selectivity of the BLM PEC sensor. The concentration of BLM was 1 μM, and the concentrations of other drugs were 10 μM. The applied potential was +0.3 V (vs. Ag/AgCl). The error bars were derived from the standard deviation of three measurements. Error bar = SD (n = 3). (B) Measurement of photocurrent for P1–Au/WS_2 probe with light on and off.

3.6. Analytical performance of the biosensor

The construction of the PEC biosensor was monitored by photocurrent output. Different concentrations of BLM·Fe^{2+} were detected under optimal conditions. As indicated from Fig. 4A, the PEC signal increased gradually with increasing the concentration of BLM·Fe^{2+} in the range of 0–10 μM. It is indicated that BLM·Fe^{2+} induced DNA strand scission is effective for detecting BLM. A good linear relationship between photocurrent density and BLM concentration can be obtained in the dynamic operating range of 0.5–500 nM (Fig. 4B) with a correlation coefficient $R^2 = 0.9912$. The linear regression equation of the calibration curve is $A = 19.41 + 0.09\ C_{BLM}$, and the limit of detection (LOD) is 0.18 nM, which is sufficiently low for pathological conditions monitoring. For comparison, the results obtained by several previously reported methods for the detection of BLM·Fe^{2+} are displayed in Table S1. Among all the methods, the PEC strategy detection limit is superior or comparable to that of the recently reported methods. It indicates that the developed PEC method exhibits good performance for BLM detection.

Selectivity and stability are important indicators for evaluating potential application value. Therefore, the determination of the selectivity and stability of BLM by biosensing platforms was studied in 10 mM Tris-HCl buffer. As indicated in Fig. 5A, the selectivity of the biosensor is investigated by comparing the photocurrent response to 1 mM BLM against that to other several antitumor drugs including daunorubicin, mitomycin and dactinomycin. Obviously, when the other antitumor drugs are added to the PEC system, the change in the PEC signal is negligible compared to the increase in the PEC signal of the sensor system after the addition of BLM (1 μM), even though at the concentration 10 times that of BLM. In addition, the photocurrent intensity of the PEC probe is almost kept constant when the visible light irradiation is repeatedly turned on (Fig. 5B). These results support the feasibility of this aptasensor for sensitive PEC assay, demonstrating that this strategy has excellent selectivity and stability for detecting BLM.

3.7. Practical analysis in serum samples

In order to evaluate the PEC biosensor potential practical application, a recovery test of BLM·Fe^{2+} in human serum was designed. The serum was provided by the Qufu Normal University School Hospital. Acetonitrile was added to the serum samples and centrifuged for 5 min (8000 rpm) before assaying eliminate potential interfering proteins in the serum. The BLM content in the samples was derived from the standard curve and the regression equation. As shown in Tables S2 and 0 nM, 10 nM, 30 nM, 50 nM and 100 nM of BLM Fe^{2+} are added into the serum samples, respectively. The recovery of BLM·Fe^{2+} is ranged from 94–110%, and the RSD is ranged from 2.1% to 3.2%, indicating the reliable application of the PEC biosensor for detection of BLM in real-life samples.

4. Conclusion

In summary, we have constructed a PEC biosensor based on nanozyme (Ag/ZnMOF) and Au/WS_2 photoelectric material for the first time, which detects BLM on the basis of Ag/ZnMOF catalytic precipitation and BLM·Fe^{2+} mediated DNA strand scission. The synthesized Au/WS_2 NA/TM possesses more active sites and generates excellent PEC signals under visible light irradiation. More importantly, the high-activity nanozyme Ag/ZnMOF composite was introduced as a signal amplifier into the PEC biosensor. It can reduce the background signal and improve the sensitivity of detection. Furthermore, on the basis of target-induced sensing strategy, the PEC signal increased with the increasing of BLM concentration. The developed PEC sensor exhibited high sensitivity and a wide linear response range (0.5–500 nM) and a low detection limit (0.18 nM) for BLM assay. The strategy had good selectivity, reproducibility and satisfactory stability. Moreover, the application of the sensor to determine BLM in human serum showed good performance. This work provides more possibilities for the PEC sensing method, and our next work will focus on the signal amplification of the sensing platform to make the PEC widely available.

Declaration of competing interest

The authors declare that they have no known competing financial interests or personal relationships that could have appeared to influence the work reported in this paper.

Acknowledgements

This work was supported by the National Natural Science Foundation of China (21775089, 51862014, 21665010), Outstanding Youth Foundation of Shandong Province (ZR2017JL010), the Key Research and Development Program of Jining City (2018ZDGH032) and Taishan scholar of Shandong Province.

Appendix A. Supplementary data

Supplementary data to this article can be found online at https://doi.org/10.1016/j.bios.2019.111875.

References

Bayer, R.A., Gaynor, E.R., Fisher, R.I., 1992. Semin. Oncol. 19, 46–52.
Bagheri, N., Khataee, A., Hassanzadeh, J., Habibi, B., 2018. J. Hazard Mater. 360, 233–242.

Claussen, C.A., Long, E.C., 1999. Chem. Rev. 99, 2797–2816.
Chen, S.Y., Yang, J.S., Wu, J.J., 2018. ACS Appl. Energy Mater. 1 (5), 2143–2149.
Cui, L., Hu, J., Wang, M., Diao, X.K., Li, C.C., Zhang, C.Y., 2018. Anal. Chem. 90, 11478–11485.
Cui, L., Yin, H., Dong, J., Fan, H., Liu, T., Ju, P., Ai, S., 2011. Biosens. Bioelectron. 26, 3278–3283.
Du, H.T., Kong, R.M., Qu, F.L., Lu, L.M., 2018. Chem. Commun. 54, 10100–10103.
Escudero, M.J., Fuerte, A., 2016. Fuel Cells 3, 340–348.
Galm, U., Hager, M.H., Van Lanen, S.G., Ju, J., Thorson, J.S., Shen, B., 2005. Chem. Rev. 105, 739–758.
Gill, G., Zayats, M., Willner, I., 2008. Angew. Chem. Int. Ed. 47, 7602–7625.
Han, Q., Wang, R., Xing, B., Chi, H., Wu, D., Wei, Q., 2018. Biosens. Bioelectron. 106, 7–13.
Hu, C., Zheng, J., Su, X., Wang, J., Wu, W., Hu, S., 2013. Anal. Chem. 85, 10612–10619.
Hao, N., Zhang, Y., Zhong, H., Zhou, Z., Hua, R., Qian, J., Liu, Q., Li, H., Wang, K., 2017. Anal. Chem. 89, 10133–10136.
Huang, Y.B., Liang, J., Wang, X.S., Cao, R., 2017. Chem. Soc. Rev. 46, 126–157.
Kong, W.S., Tan, Q.Q., Guo, H.Y., Sun, H., Qin, X., Qu, F.L., 2019. Microchim. Acta 186, 73–80.
Kelly, K.L., Coronado, E., Zhao, L.L., Schatz, G.C., 2003. J. Phys. Chem. B 107, 668–677.
Li, Y., Huang, C.C., Zheng, J.B., Qi, H.L., Cao, W., Wei, Y.M., 2013. Biosens. Bioelectron. 44, 177–182.
Li, M.J., Xiong, C., Zheng, Y.N., Liang, W.B., Yuan, R., Chai, Y.Q., 2018. Anal. Chem. 90, 8211–8216.
Liu, S.S., He, P., Hussain, S., Lu, H., Zhou, X., Lv, F.T., Liu, L.B., Dai, Z.H., Wang, S., 2018. ACS Appl. Mater. Interfaces 10, 6618–6623.
Li, M.J., Zheng, Y.N., Liang, W.B., Yuan, Y.L., Chai, Y.Q., Yuan, R., 2016. Chem. Commun. 52, 8138–8141.
Liu, P., Huo, X., Tang, Y., Xu, J., Liu, X., Wong, D.K.Y., 2017. Anal. Chim. Acta 984, 86–95.
Liu, Z., Hou, W., Pavaskar, P., Aykol, M., Cronin, S., 2011. Nano Lett. 11, 1111–1116.
Li, B., Gu, T., Ming, T., Wang, J., Wang, P., Wang, J., Yu, J., 2014. ACS Nano 8, 8152–8162.
Li, B., Chrzanowski, M., Zhang, Y., Ma, S., 2016. Coord. Chem. Rev. 307, 106–129.
Li, R.Y., Tu, W.W., Wang, H.S., Dai, Z.H., 2018. Anal. Chem. 90, 9403–9409.
Lim, Y.V., Wang, Y., Kong, D., Guo, L., Wong, J.I., Anga, L.K., Yang, H.Y., 2017. J. Mater. Chem. A 5, 10406–10415.
Ma, L., Han, X., Xia, L., Kong, R.M., Qu, F.L., 2018. Analyst 143, 5474–5480.
Ma, Z.Y., Ruan, Y.F., Xu, F., Zhao, W.W., Xu, J.J., Chen, H.Y., 2016. Anal. Chem. 88, 3864–3871.
Ma, Z.Y., Ruan, Y.F., Zhang, N., Zhao, W.W., Xu, J.J., Chen, H.Y., 2015. Chem. Commun. 51, 8381–8384.
Pu, Z., Liu, Q., Asiri, A.M., Obaid, A.Y., Sun, X., 2014. Electrochim. Acta 134, 8–12.
Ren, X., Ge, R., Zhang, Y., Liu, D., Wu, D., Sun, X., Du, B., Wei, Q., 2017. J. Mater. Chem. A 5, 7291–7294.
Stubbe, J., Kozarich, J.W., 1987. Chem. Rev. 87, 1107–1136.
Sleijfer, S., 2001. Chest 120, 617–624.
Seh, Z.W., Liu, S., Low, M., Zhang, S., Liu, Z., Mlayah, A., Han, M., 2012. Adv. Mater. 24, 2310–2314.
Tang, J., Zhang, Y., Kong, B., Wang, Y., Da, P., Li, J., Elzatahry, A.A., Zhao, D., Gong, X., Zheng, G., 2014. Nano Lett. 14, 2702–2708.
Wang, H.H., Li, M.J., Zheng, Y.N., Hu, T., Chai, Y.Q., Yuan, R., 2018. Biosens. Bioelectron. 120, 71–76.
Wang, G.L., Yuan, F., Gu, T.T., Dong, Y.M., Wang, Q., Zhao, W.W., 2018. Anal. Chem. 90, 1492–1497.
Wu, R., Fan, G.C., Jiang, L.P., Zhu, J.J., 2018. ACS Appl. Mater. Interfaces 10, 4429–4438.
Wang, C.I., Chen, W.T., Chang, H.T., 2012. Anal. Chem. 84, 9706–9712.
Wen, T., Zhang, D.X., Liu, J., Zhang, H.X., Zhang, J., 2015. Chem. Commun. 51, 1353–1355.
Wu, Z., Fang, B., Bonakdarpour, A., Sun, A., Wilkinson, D.P., Wang, D., 2012. Appl. Catal. B Environ. 125, 59–66.
Yin, B.C., Wu, D., Ye, B.C., 2010. Anal. Chem. 82, 8272–8277.
You, D., Xu, C., Wang, J., Su, W., Zhang, W., Zhao, J., Liu, Y., 2018. ACS Appl. Mater. Interfaces 10 (41), 35184–35193.
Yan, Z., Wang, Z., Miao, Z., Liu, Y., 2016. Anal. Chem. 88, 922–929.
Yan, R., Bao, J., Tu, W., Dai, Z., 2016. Chem. Commun. 52, 11799–11802.
Zhao, Y., Zheng, Y.Q., Kong, R.M., Xia, L., Qu, F.L., 2016. Biosens. Bioelectron. 75, 383–388.
Zhang, L., Ruan, Y.F., Liang, Y.Y., Zhao, W.W., Yu, X.D., Xu, J.J., Chen, H.Y., 2018. ACS Appl. Mater. Interfaces 10, 3372–3379.
Zhu, Y.C., Xu, Y.T., Xue, Y., Fan, G.C., Zhang, P.K., Zhao, W.W., Chen, H.Y., 2019. Anal. Chem. 91 (10), 6419–6423.
Zhang, C.Y., Wang, S., Yang, L.J., Liu, Y., Xu, T.T., Ning, Z.Y., Zak, A., Zhang, Z.Y., Tenne, R., Chen, Q., 2012. Appl. Phys. Lett. 100, 243101.
Zou, J.P., Ma, J., Luo, J.M., Yu, J., He, J., Meng, Y., Luo, Z., Bao, S.K., Liu, H.L., Luo, S.L., Luo, X.B., Chen, T.C., 2015. Appl. Catal. B Environ. 179, 220–228.